Bright and dark solitons in the systems with strong light-matter coupling: Exact solutions and numerical simulations

A. V. Yulin and D. A. Zezyulin*
School of Physics and Engineering, ITMO University, St. Petersburg 197101, Russia

(Received 16 May 2022; accepted 19 September 2022; published 10 October 2022)

We theoretically study bright and dark solitons in an experimentally relevant hybrid system characterized by strong light-matter coupling. We find that the corresponding two-component model supports a variety of coexisting moving solitons including bright solitons on zero and nonzero background and dark-gray and gray-gray solitons. The solutions are found in the analytical form by reducing the two-component problem to a single stationary equation with cubic-quintic nonlinearity. All found solutions coexist under the same set of the model parameters, but, in a properly defined linear limit, approach different branches of the polariton dispersion relation for linear waves. Bright solitons with zero background feature an oscillatory-instability threshold which can be associated with a resonance between the edges of the continuous spectrum branches. "Half-topological" dark-gray and nontopological gray-gray solitons are stable in wide parametric ranges below the modulational instability threshold, while bright solitons on the constant-amplitude pedestal are unstable.

DOI: 10.1103/PhysRevE.106.044202

I. INTRODUCTION

Optical solitons, such as localized waves propagating in nonlinear fibers, were predicted [1] and experimentally observed [2] more than 40 years ago. Since then optical solitary waves have been discovered and thoroughly studied in many optical systems. Apart from the fundamental importance, optical solitons can also be of interest from practical point of view, in particular, for information transmission and supercontinuum generation [3–5]. To describe formation of solitons, it is necessary to combine Maxwell equations with the equations accounting for the response of the material to the propagating electromagnetic field. This description is, however, in many cases so complicated that even numerical modeling of the dynamics of the light becomes impossible. Fortunately, the presence of small parameters often allows one to simplify the problem. For example, slow-varying amplitude approximation has proven to be a very powerful and precise model which allows one to describe a large variety of optical phenomena using the nonlinear Schrödinger (NLS) equation and a family of its generalizations [6,7]. In its basic form, the NLS equation is fully integrable and its soliton solutions are available in the analytical form. The knowledge of exact soliton solution for the NLS equation and other prototypical nonlinear models has twofold importance. First, it helps to understand the properties of the localized waves in the considered system and, in particular, facilitates the stability study. Second, the analytical solutions can be used as a starting point for the development of a perturbation theory for more complex and general systems which take into account the originally neglected effects and do not always admit analytical solutions.

In this paper, we address bright and dark solitons propagating in optical waveguides with strong light-matter coupling which is a typical attribute of exciton-polariton systems. The system of such a kind consists of a dielectric waveguide with built-in quantum wells supporting excitons. If the losses are small, then, at the frequencies close to the exciton resonance, the photons and the excitons interact strongly so that at the crossing point the dispersions of the photons and the excitons hybridize and get split forming the lower and the upper polariton branches.

Without resonant material excitations, the nonlinear effects usually come to play at so high pulse energies that it reduces its practical applicability, especially in optical on-chip devices. The effective (material and waveguide) dispersion is also relatively low in these systems. For example, typical energy of 100 fs optical solitons in highly nonlinear optical waveguides is of the order of 100 pJ, and the soliton formation occurs at propagation distances of several centimeters. The advantage of the systems with strong light-matter coupling is that because of the material component of the eigenmodes the nonlinear effects are orders of magnitude stronger than in the systems with weak coupling. Another important fact is that the typical dispersion caused by the linear photon-exciton interaction is much stronger compared to the dispersion of pure photons. This allows one to observe soliton formation at the propagation distances of order of hundreds microns and the energy of order of hundreds of fJ in 100 fs pulses. This makes the systems with strong light-matter interaction to be very promising for studying different nonlinear effects and explains why these systems have been attracting so much of attention over the recent years [8].

The simplest model describing the dynamics of pulses propagating in the waveguides with strong light-matter interaction neglects the dispersion and nonlinearity of pure photons, and hence the photonic component is described by a linear equation. This equation is coupled to the equation for excitons where the resonant frequency of the excitons is a

*d.zezyulin@gmail.com

function of their density. In the simplest case considered herein, the shift of the exciton frequency is proportional to their density. In the context of mean-field approximation for polariton systems, the corresponding model was introduced in [9] and has been widely used. The adaptation of the model for the case when the frequency of excitation is much higher than the cutoff frequency of the waveguide is done in [10]. The latter model can be brought to the following form:

$$i(\partial_t A + \partial_x A) = -\kappa\psi, \quad i\partial_t\psi = -\kappa A + g|\psi|^2\psi. \quad (1)$$

Here t is the time normalized on some characteristic frequency Ω_0, x is the coordinate normalized on the Ω_0/v_g, v_g is the group velocity of the pure photon mode at the resonant frequency of the material excitations Ω_m. In Eqs. (1) the coefficient κ accounts for the light-matter coupling strength and without loss of generality can be set to 1. This means that the normalization frequency Ω is chosen to be equal to the light-matter coupling in the system.

The function $A(x,t)$ in (1) is the slow-varying amplitude of the photon field and $\psi(x,t)$ is the order parameter describing the material excitations; for example, ψ can be the order parameter of the coherent excitons in a semiconductor microcavity. To achieve analytical solutions, we disregard the dispersion of the pure guided photons assuming this is much smaller compared to the dispersion appearing due to the light-matter coupling (as it is typical for experimental conditions [10]). The effective mass of the coherent excitons is supposed to be much greater than the effective mass of guided photons (for semiconductor microcavities the typical values $<10^{-4}$), and thus the frequency of linear material excitations does not depend on their wave vector. Let us remark that all frequencies used below in this paper are actually the detunings of the frequency from the linear frequency of the material excitations Ω_m. The wave vectors, in their turn, are the detunings of the wave vectors from the wave vector of the pure photonic mode of the frequency Ω_m.

Normally in the systems with strong light-matter coupling the dominating nonlinearity originates from the resonant frequency dependency of the material excitations on their density. In our model this frequency shift is taken to be proportional to the density of the material excitations and thus is equal to $g|\psi|^2$. Aiming to obtain analytical solutions, we consider a conservative problem. The conservative limit is a good approximation for polariton waves propagating over the distances sufficient to observe the formation of the solitons (hundreds of microns). The comprehensive studies of the effect of losses is definitely of interest but is out of the scope of the present paper and will be done elsewhere.

In the linear limit $g = 0$, for plane-wave solutions $\propto e^{-i\delta t+ikx}$, where δ is the frequency and k is the wave number, we obtain two polariton branches (upper, with subscript 1, and lower, with subscript 2) of the dispersion relation (plotted in Fig. 1):

$$\delta_{1,2}(k) = (k \pm \sqrt{k^2 + 4\kappa^2})/2. \quad (2)$$

System (1) can be reduced to the NLS equation written for the amplitude of the polariton mode belonging either to the lower or the upper branch provided the peak power of the pulse causes the exciton frequency shift much less compared to width of the gap between the upper and the lower polariton branches. However, the soliton of higher intensities have to be considered taking into account the dispersion of the nonlinearity and the excitations belonging to both branches. That is why the analysis of the full two-component model is important. We also note that a generalized version of model (1) has been used to describe the formation of dark solitons in polariton fluids [11]. Another pertinent remark is that system (1) is mathematically similar to the coupled-mode equations describing gap solitons in optical fibers with grating [12]. The importance difference is that in (1) only the equation for ψ field (order parameter function describing coherent polaritons) is nonlinear whereas in the case of gap solitons both fields are nonlinear.

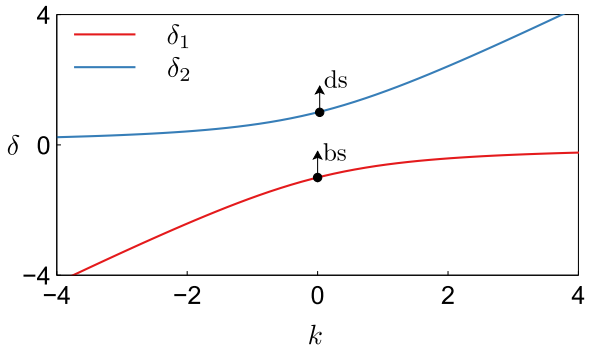

FIG. 1. Dispersion relation for linear waves $\delta_{1,2}$ given by (2). Arrows labeled "bs" and "ds" correspond to the frequencies of, respectively, bright and dark solitons detaching from the polariton branches. Direction of arrows corresponds to the increase of the soliton amplitudes.

It has been found in [10] that system (1) admits an analytical bright soliton solution whose existence has been confirmed experimentally. In this paper, we perform a comprehensive study of different kinds of bright and dark solitons existing in the system and look into stability of the found analytical solitons. We find that apart from the bright solitons, the system admits "semitopological" dark-gray solitons, nontopological gray-gray solitons, and bright solitons nestling in the background of nonzero constant amplitude. All these solutions, which are found in the analytical form, coexist in the system with the same set of model parameters. At the same time, in a properly defined linear limit, the frequency and wave vector of bright solitons approach the lower-frequency branch of the dispersion relation, while solitons of other types approach the upper polariton branch. We numerically observe that large-amplitude bright solitons are prone to oscillatory instabilities which, however, can have rather weak instability increment. Dark-gray and gray-gray solutions are stable in a vast range of parameters. The stability predictions are verified with direct numerical modeling of soliton dynamics.

The rest of our paper is organized as follows. In Sec. II we present the analytical exact solutions for bright and dark solitons and discuss their spectral stability. In Sec. III we present the result of direct numerical modeling of soliton dynamics. Section IV concludes the paper.

II. EXACT MOVING SOLITON SOLUTIONS

A. Construction of solutions

We are looking for soliton solutions in the moving frame $\zeta = x - v_s t$, where v_s is the velocity (hereafter, the subscript "s" stands for "soliton"). We therefore introduce the following substitutions: $A(x,t) = A_s(\zeta)e^{-i\delta_s t}$, and $\psi(x,t) = \psi_s(\zeta)e^{-i\delta_s t}$. The solitons are characterized by two parameters: velocity v_s and frequency in the moving frame δ_s (which is generically different from the frequency δ in the laboratory frame). Then system (1) reduces to

$$i(1-v_s)A_s' + \delta_s A_s = -\kappa\psi_s, \tag{3}$$

$$-iv_s\psi_s' + \delta_s\psi_s = -\kappa A_s + g|\psi_s|^2\psi_s, \tag{4}$$

where the prime means derivative with respect to the moving frame coordinate ζ. Differentiating the second equation of the latter system one more time, one can eliminate the wave function $A_s(\zeta)$ and reduce the system to a single equation for $\psi_s(\zeta)$. Using a substitution

$$\psi_s(\zeta) = \phi_s(\zeta)\exp\left[-i\zeta\frac{\delta_s(1-2v_s)}{2v_s(1-v_s)}\right], \tag{5}$$

where $\phi_s(\zeta)$ is a new unknown, the problem transforms to

$$-v_s^2\phi_s'' + \left[\frac{\kappa^2 v_s}{1-v_s} - \frac{\delta_s^2}{4(1-v_s)^2}\right]\phi_s + \frac{g\delta_s}{2(1-v_s)}|\phi_s|^2\phi_s + igv_s(|\phi_s|^2\phi_s)' = 0. \tag{6}$$

Next, we use the polar form $\phi_s(\zeta) = \rho_s(\zeta)e^{i\Theta_s(\zeta)}$ and decompose Eq. (6) into real and imaginary parts. The latter results in the following relation:

$$\Theta_s'\rho_s^2 = \frac{3g}{4v_s}\rho_s^4 + C, \tag{7}$$

where C is arbitrary constant of integration. Then the real part of the polar decomposition becomes

$$-v_s^2\rho_s'' + \left[\frac{\kappa^2 v_s}{1-v_s} - \frac{\delta_s^2}{4(1-v_s)^2} + \frac{gCv_s}{2}\right]\rho_s + \frac{g\delta_s}{2(1-v_s)}\rho_s^3 - \frac{3g^2}{16}\rho_s^5 + \frac{C^2v_s^2}{\rho_s^3} = 0. \tag{8}$$

In the particular case $C = 0$ the latter equation can be considered as a stationary version of the cubic-quintic nonlinear Schrödinger equation, which is known to support a number of solutions in the form of bright and dark solitons, many of which can be found in the analytical form; see, e.g., [6,7,13]. This observation paves the way towards the systematic construction of analytical solitons for the original system (1). The quintic nonlinearity in (8) is focusing, while sign and effective strength of the cubic nonlinearity depend on both the soliton velocity v_s and frequency δ_s.

Types of existing solutions can be also anticipated from the phase portrait which can be obtained by multiplying Eq. (8) by ρ_s' and integrating. Representative phase portraits for different combinations of the parameters are presented in Fig. 2. For $C = 0$ and different values of the frequency δ_s the system admits homoclinic orbits which join the equilibrium

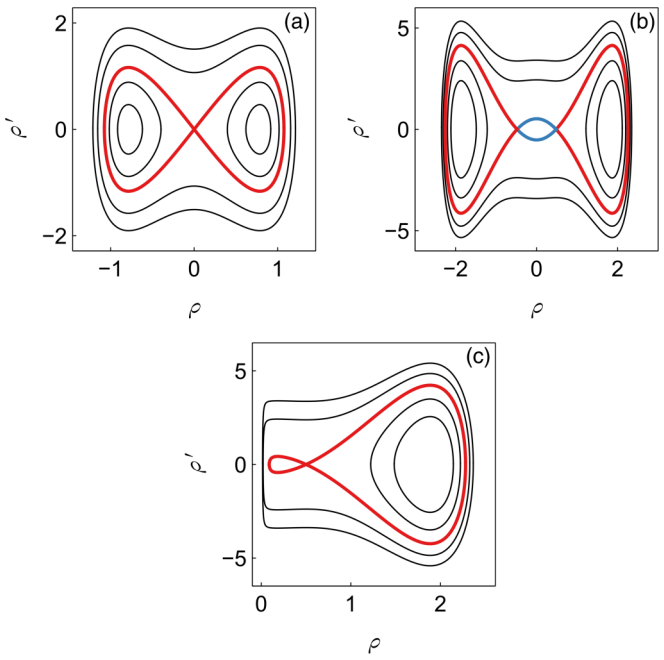

FIG. 2. Phase portraits of Eq. (8) obtained for $\kappa = g = 1$, $v_s = 0.25$, $\delta_s \approx -0.433$ (a), $\delta_s \approx 1.044$ (b), and $\delta_s = 1.07$ (c). Trajectories corresponding to homo- and heteroclinic orbits are highlighted with red and blue, respectively. In upper panels $C = 0$, and in the lower panel $C \approx 0.051$.

$(\rho_s, \rho_s') = (0,0)$ to itself and hence correspond to bright solitons [Fig. 2(a)] or homoclinic orbits corresponding to bright solitons situated on a nonzero background coexisting with and heteroclinic orbits corresponding to dark solitons [Fig. 2(b)]. For nonzero C [Fig. 2(c)], the system has homoclinic orbits of different types that correspond to bright solitons on a nonzero background (with maximal amplitude larger than that of the equilibrium) and to gray solitons (i.e., dips in the uniform background).

If the amplitude $\rho_s(\zeta)$ is found from Eq. (8), one can recover the argument $\Theta_s(\zeta)$ of the corresponding excitonic field using (7) and then find the photonic component $A_s(\zeta)$ from Eq. (4). In the particular case $C = 0$ for the amplitude of the photonic field we compute

$$|A_s(\zeta)|^2 = \frac{v_s}{1-v_s}\left(\rho_s^2(\zeta) - \rho_\infty^2\right) + \frac{\rho_\infty^2}{\kappa^2}\left[\frac{g}{4}\rho_\infty^2 - \frac{\delta_s}{2(1-v_s)}\right]^2, \tag{9}$$

where constant ρ_∞ is determined by the boundary conditions

$$\lim_{\zeta\to\infty}\rho_s^2(\zeta) = \lim_{\zeta\to-\infty}\rho_s^2(\zeta) =: \rho_\infty^2, \tag{10}$$

$$\lim_{\zeta\to\infty}\rho_s'(\zeta) = \lim_{\zeta\to-\infty}\rho_s'(\zeta) = 0. \tag{11}$$

Therefore the squared amplitudes of $\psi_s(\zeta)$ and $A_s(\zeta)$ are proportional, except for an additive constant which is determined by the asymptotic behavior at the infinities.

B. Bright solitons

As is evident from Fig. 2(a), for $C = 0$ in Eq. (8) the system supports bright solitons for which $\rho_\infty = 0$ in boundary conditions (10). As follows from (9) with $\rho_\infty = 0$, solutions of this type can only be meaningful for $v_s \in (0, 1)$. Bright soliton solutions can be written down in the compact form if ones introduces two auxiliary angles $\alpha \in (0, \pi/2)$ and $\theta \in (-\pi/2, \pi/2)$ and adopts the following parametrization for the soliton frequency and velocity:

$$v_s = \sin^2\alpha, \quad \delta_s = -\kappa \sin(2\alpha)\sin\theta. \tag{12}$$

Then the following solution can be found (see also [10]):

$$\begin{aligned}\psi_s(\zeta) &= \rho_s(\zeta) e^{2i\zeta\kappa\cot(2\alpha)\sin\theta + i\Theta_s(\zeta)},\\ A_s(\zeta) &= \tan(\alpha)\rho_s(\zeta) e^{2i\zeta\kappa\cot(2\alpha)\sin\theta + i\Theta_s(\zeta)/3},\end{aligned} \tag{13}$$

where

$$\begin{aligned}\rho_s^2(\zeta) &= \frac{4\kappa}{g}\frac{\tan\alpha\cos^2\theta}{\sin\theta + \cosh[4\kappa\cos\theta\csc(2\alpha)\zeta]},\\ \Theta_s(\zeta) &= 3\arctan\left\{\frac{1-\sin\theta}{\cos\theta}\tanh[2\kappa\cos\theta\csc(2\alpha)\zeta]\right\}.\end{aligned} \tag{14}$$

Since bright solitons (13)–(14) are found in the frame moving with velocity v_s, the frequency in the laboratory frame amounts to $\delta = \delta_s + 2v_s\kappa\cot(2\alpha)\sin\theta = -\kappa\sin\theta\tan\alpha$, and the spatial wavenumber of soliton tails amounts to $k_s = 2\kappa\cot(2\alpha)\sin\theta$. In the limit $\theta \to \pi/2$ the soliton amplitude tends to zero, and the solution frequency δ approaches from above the lower branch of the dispersion relation, i.e., $\delta = \delta_1(k_s)$, where the polariton dispersion laws $\delta_{1,2}(k)$ are defined in (2). This is shown schematically with the arrow "bs" in Fig. 1. In the limit $\theta \to -\pi/2$, the solution frequency approaches (from below) the upper polariton branch $\delta_2(k)$. In this limit, the shape of the solution becomes algebraic:

$$\lim_{\theta\to-\pi/2}\rho_s^2(\zeta) = \frac{16\kappa}{g}\frac{\sin(2\alpha)\sin^2\alpha}{\sin^2(2\alpha) + 16\kappa^2\zeta^2}. \tag{15}$$

Let us now look into stability of the found bright gap solitons. Using the standard linear stability analysis, we consider perturbed stationary solutions in the form

$$A(x,t) = e^{-i\delta_s t}[A_s(\zeta) + a_1(\zeta)e^{\lambda t} + a_2^*(\zeta)e^{\lambda^* t}], \tag{16}$$

$$\psi(x,t) = e^{-i\delta_s t}[\psi_s(\zeta) + p_1(\zeta)e^{\lambda t} + p_2^*(\zeta)e^{\lambda^* t}], \tag{17}$$

where $a_{1,2}(\zeta)$ and $p_{1,2}(\zeta)$ describe the spatial shapes of the perturbations, and and complex λ characterizes the temporal behavior of the perturbations (positive real part of λ means that the perturbations grow and the soliton is therefore unstable). Substituting these expressions in Eq. (1) and keeping only linear (with respect to the small perturbations) terms, we arrive at the following system of linear stability equations which can be treated as an eigenvalue problem for the instability increment λ:

$$\begin{aligned}i\lambda a_1 &= -i(1-v_s)a_1' - \delta_s a_1 - \kappa p_1,\\ i\lambda a_2 &= -i(1-v_s)a_2' + \delta_s a_2 + \kappa p_2,\\ i\lambda p_1 &= -\kappa a_1 + iv_s p_1' - (\delta_s - 2g|\psi_s|^2)p_1 + g\psi_s^2 p_2,\\ i\lambda p_2 &= \kappa a_2 - g(\psi_s^*)^2 p_1 + iv_s p_2' + (\delta_s - 2g|\psi_s|^2)p_2.\end{aligned} \tag{18}$$

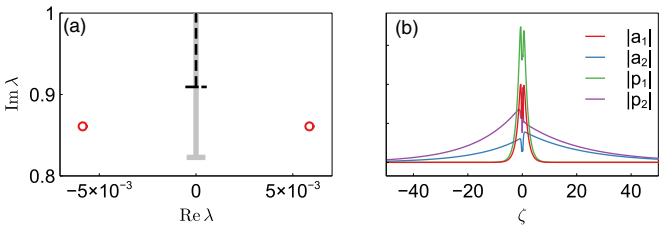

FIG. 3. (a) A pair of complex eigenvalues λ and $-\lambda^*$ (shown with circles) found numerically in the vicinity of the nearly resonant edges of the continuous spectrum for small negative θ. Two partially overlapping branches of the continuous spectrum are shown with vertical solid gray and dotted black lines, and the edges of the branches are emphasized with short horizontal bars. There also exist a pair of eigenvalues $-\lambda$ and λ^* in the lower half-plane, not shown in the figure. (b) Spatial profile of the corresponding four-component eigenvector. In this figure, $g = \kappa = 1$, $\alpha = \pi/6$, and $\theta = -0.05$.

It is known that dynamics of gap solitons in various setups can be affected by *oscillatory instabilities* (OIs) which correspond to unstable eigenvalues detaching from the edges of the continuous spectrum [7,14,15]. By definition [7], the instability of this type is associated with a quartet of complex eigenvalues $(\pm\lambda, \pm\lambda^*)$; see panel "OI" in Fig. 4. Another common type of instabilities corresponds to a pair of purely real eigenvalues $(\lambda, -\lambda)$. The instability of this type can be referred to as the *internal* or *exponential instability* (EI); see schematic illustration "OI and EI" in Fig. 4.

We solve the eigenvalue problem (18) by approximating the derivatives by finite differences and evaluating the spectrum of the resulting sparse matrix using the MatLab eigs procedure. The fourth-order approximation has been used for the derivatives subject to the zero boundary conditions. Depending on the localization of eigenfunctions, we have used different computational windows $\zeta \in [-L, L]$, with L ranging from 20 to 160 and number of grid nodes ranging from 10^4 to 2×10^4. In each case it has been checked that small variations of the grid parameters do not have any essential impact on the outcomes of the computation. Numerical solution of the linear stability eigenvalue problem (18) indicates

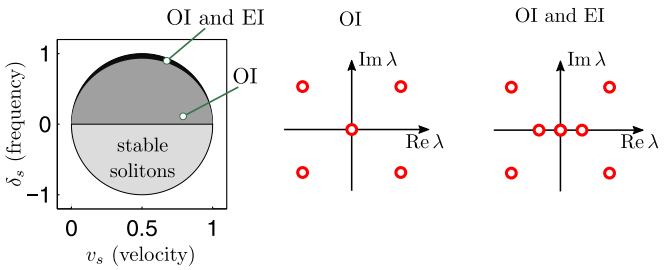

FIG. 4. Left panel shows the existence and stability diagram for bright solitons on the plane (δ_s, v_s) for $g = \kappa = 1$. The light-gray domain corresponds to stable solitons, the dark-gray domain corresponds to solitons with oscillatory instabilities (OIs), and the black sickle-shaped region corresponds to high-frequency solitons with coexisting oscillatory and purely exponential instabilities (OIs and EIs). In the white domain bright solitons do not exist. Two panels on the right show schematically the location of unstable eigenvalues for the two situations.

that the oscillatory instabilities are indeed present in our system. More specifically, we observe that solitons with $\delta_s < 0$ are stable, whereas oscillatory instabilities can be found for $\delta_s > 0$. Precise detection of the instability threshold is a numerically challenging problem, because for δ_s close to zero the instability increments are rather weak, and the decay of the tails of corresponding unstable eigenmodes is extremely slow as ζ approaches ∞ and $-\infty$. At the same time, the stability change at $\delta_s = 0$ [which, in terms of parametrization (12), corresponds to $\theta = 0$] can be anticipated as one looks at the continuous spectrum associated with the linear stability system (18). It has four branches of the continuous spectrum that occupy the following intervals of the imaginary axis:

$$\lambda_{1,2} \in i[\kappa \sin(2\alpha)(1 \pm \sin\theta), +\infty), \tag{19}$$

$$\lambda_{3,4} \in (-\infty, -\kappa \sin(2\alpha)(1 \pm \sin\theta)]i. \tag{20}$$

Exactly at $\theta = 0$ the edges of the continuous spectrum coincide pairwise and become resonant, which, as we conjecture, results in the bifurcation of a quartet of oscillatory instability eigenvalues, with two eigenvalues emerging from $\lambda = i\kappa \sin(2\alpha)$ and two more eigenvalues emerging from $\lambda = -i\kappa \sin(2\alpha)$. Weak oscillatory instabilities (with the instability increment $\mathrm{Re}\,\lambda \lesssim 10^{-2}$) emerging in the vicinity of the resonant spectrum edges have indeed been observed in our numerical simulations for small positive δ_s as shown in Fig. 3. As δ_s increases towards larger positive values, the increment of oscillatory instability grows.

As pointed out above in this section, apart from the oscillatory instabilities, the system can admit purely exponential instabilities associated with a pair of purely real eigenvalues $\pm\lambda \in \mathbb{R}$ in the linearization spectrum. The instability of this type emerges at the moment when two stable internal modes (i.e., purely imaginary and complex-conjugate eigenvalues) collide at the origin and then split into a pair of purely real eigenvalues of opposite sign. The moment of such an eigenvalue zero crossing can be obtained analytically using the multiple-scale analysis [14,16]. To this end, we notice that the system (1) with zero boundary conditions has two conserved quantities: $Q = \int_{-\infty}^{\infty} dx(|A|^2 + |\psi|^2)$ and $P = \frac{i}{2}\int_{-\infty}^{\infty} dx(A\partial_x A^* - A^*\partial_x A + \psi\partial_x\psi^* - \psi^*\partial_x\psi)$. For bright solitons given by the exact solution (13), these quantities become functions of α and θ:

$$Q_s = \frac{2\tan^2\alpha}{g}(\pi - 2\theta), \tag{21}$$

$$P_s = \frac{4\kappa\tan\alpha}{g\cos^2\alpha}[(1 + 2\cos^2\alpha)\cos\theta - (\pi - 2\theta)\sin\theta]. \tag{22}$$

The multiple-scale analysis relies on the assumption that if the increment of the newly emerged exponential instability is small, then the initial stage of the dynamical instability development results in the adiabatic change of the solitons frequency and velocity, i.e., one can introduce functions $v_s = v_s(T)$ and $\delta_s = \delta_s(T)$, where $T = \epsilon t$ is a "slow time," and ϵ is a formal small parameter. Respectively, the auxiliary parameters are also to be considered as function of the slow time: $\alpha = \alpha(T)$ and $\theta = \theta(T)$. Carrying out the corresponding calculations, we observe that a new small unstable eigenvalue appears in (or disappears from) the linearization spectrum at the instance when the following condition is satisfied:

$$\frac{\partial P_s}{\partial\alpha}\frac{\partial Q_s}{\partial\theta} - \frac{\partial P_s}{\partial\theta}\frac{\partial Q_s}{\partial\alpha} = 0. \tag{23}$$

Direct computation reduces (23) to the following simple equation for θ:

$$(\pi^2 - 4\pi\theta + 4\theta^2 - 3)\cos\theta + 2(\pi - 2\theta)\sin\theta = 0. \tag{24}$$

Within the interval $\theta \in (-\pi/2, \pi/2)$, the latter equation has a single root $\theta_\star \approx -1.189$, with $\sin\theta_\star \approx -0.928$. In terms of the soliton frequency and velocity, the found threshold corresponds to the following dependence:

$$\delta_{s,\star} = -2\kappa\sqrt{v_s(1 - v_s)}\sin\theta_\star = -\kappa\sin(2\alpha)\sin\theta_\star. \tag{25}$$

The emergence of a new pair of real eigenvalues as the soliton frequency δ_s increases above the found threshold value $\delta_{s,\star}$ has been verified by means of direct evaluation of the linear stability eigenvalues. At the same time, since $\delta_{s,\star}$ is well above zero, these new eigenvalues emerge in the parametric region where the bright solitons are *already* unstable due to the oscillatory instabilities described above. Therefore, for a generic initial perturbation, this additional exponential instability has no significant impact on the overall behavior of the system.

Results of the stability analysis for bright solitons are summarized in the diagram shown in Fig. 4. It shows the domain of existence of bright solitons on the plane (δ_s, v_s) and demarcates the stability and instability regions.

C. Dark-gray solitons and bright solitons on a nonzero pedestal

Phase portrait shown in Fig. 2(b) indicates that for $C = 0$ and sufficiently large frequencies δ_s the system supports solitons of two more types. First, the heteroclinic orbit in Fig. 2(b) correspond to dark solitons for which the profile $\rho_s(\zeta)$ increases monotonically from $-\rho_\infty$ to $+\rho_\infty$ and becomes zero at some ζ, where the excitonic wave function $\psi_s(\zeta)$ has a topological π phase jump. Regarding the corresponding photonic field $A_s(\zeta)$, from (9) we observe that for $v_s \in (0, 1)$ the amplitude $|A_s|^2$ corresponds to a dip in the uniform background. Moreover, the amplitude of the wave function nowhere vanishes, i.e., $|A_s(\zeta)| > 0$ for all ζ, i.e., corresponds to a nontopological (gray) soliton without the phase jump.

The second type of soliton solutions in the phase portrait Fig. 2(b) corresponds to bright solitons on nonzero pedestal. For these solutions both fields $\psi_s(\zeta)$ and $A_s(\zeta)$ correspond to humps on the constant-amplitude background.

To present these solutions, for $v_s \in (0, 1)$ it is convenient to introduce the following parametrization:

$$v_s = \sin^2\alpha, \quad \delta_s = \frac{\kappa}{2}\sin(2\alpha)(3e^{\theta} - e^{-\theta}), \tag{26}$$

where $\alpha \in (0, \pi/2)$ and $\theta > 0$, and the following constants:

$$\rho_\infty^2 = \frac{4\kappa}{g}\tan\alpha\sinh\theta, \qquad b = \frac{1}{4}(1 - e^{-2\theta}),$$
$$p = \kappa\csc(2\alpha)\sqrt{3e^{2\theta} - e^{-2\theta} - 2}. \tag{27}$$

Then the dark soliton profile reads

$$\psi_s(\zeta) = \rho_s(\zeta) e^{-i\kappa(3e^{\theta}-e^{-\theta})\cot(2\alpha)\zeta + i\Theta_s(\zeta)}, \tag{28}$$

where

$$\rho_s(\zeta) = \frac{\rho_\infty \sinh(p\zeta)}{\sqrt{\cosh^2(p\zeta) - b}}, \tag{29}$$

$$\Theta_s(\zeta) = 6\kappa \sinh\theta \csc(2\alpha)\zeta - 3\arctan\left[\sqrt{\frac{1-e^{-2\theta}}{3+e^{-2\theta}}}\tanh(p\zeta)\right]. \tag{30}$$

For bright solitons on the background, it is sufficient to redefine

$$b = (3 + e^{-2\theta})/4, \tag{31}$$

and the resulting solution is obtained from (28) with

$$\rho_s(\zeta) = \frac{\rho_\infty \cosh(p\zeta)}{\sqrt{\cosh^2(p\zeta) - b}}, \tag{32}$$

$$\Theta_s(\zeta) = 6\kappa \sinh\theta \csc(2\alpha)\zeta - 3\arctan\left[\sqrt{\frac{1-e^{-2\theta}}{3+e^{-2\theta}}}\coth(p\zeta)\right] + 3\pi/2, \tag{33}$$

where (33) is only valid for $\zeta \geqslant 0$, and for $\zeta < 0$ the argument must be redefined as an odd function, i.e., $\Theta_s(\zeta) := -\Theta_s(-\zeta)$.

The frequency in the laboratory frame can be computed from the soliton frequency as $\delta = -\kappa(3e^{\theta} - e^{-\theta})\cot(2\alpha)v_s + \delta_s = (\kappa/2)(3e^{\theta} - e^{-\theta})\tan\alpha$. For dark solitons, it is natural to define the small-amplitude limit as $\rho_\infty \to 0$, which in the case at hand corresponds to $\theta \to +0$. In this limit the frequency δ approaches the upper polariton branch of the dispersion relation from above as shown schematically with arrow "ds" in Fig. 1.

Before we proceed to stability of the found solutions, it is important to examine the potential *modulational instability* [7] of the corresponding constant-amplitude background. Far from the soliton core, the solutions asymptotically transform to constant-ampltidude waves $\psi_0(\zeta) = \rho_\infty e^{i\Omega\zeta}$, where

$$\Omega = \kappa \csc(2\alpha)[6\sinh\theta - (3e^{\theta} - e^{-\theta})\cos(2\alpha)]. \tag{34}$$

For these constant-amplitude solutions, we perform the standard modulational stability analysis using a substitution similar to (16) with perturbations $a_{1,2}(\zeta) = \tilde{a}_{1,2}e^{\pm i\Omega\zeta + ik\zeta}$, $p_{1,2}(\zeta) = \tilde{p}_{1,2}e^{\pm i\Omega\zeta + ik\zeta}$, where $\tilde{a}_{1,2}$ and $\tilde{p}_{1,2}$ are constants, and real k characterizes the the wave number of the perturbation. Then the modulational instability eigenvalues $\lambda(k)$ can be found as roots of a quartic characteristic equation. The exhaustive classification of all roots is a tedious task, but it is possible to describe their behavior the limit $k \to \infty$. Using computer algebra, one can show, that in this limit the roots of the characteristic equation have asymptotic behavior as follows:

$$\lambda_{1,2}(k) = ik\cos^2\alpha - ic_{1,2} + o(1), \tag{35}$$

$$\lambda_{3,4}(k) = -ik\sin^2\alpha - ic_{3,4} + o(1), \tag{36}$$

where

$$c_{1,2} = \pm\kappa e^{-\theta}\cot\alpha, \quad c_{3,4} = \pm\kappa\tan\alpha\sqrt{4 - 3e^{2\theta}}. \tag{37}$$

Therefore the coefficients $c_{1,2}$ are real, while $c_{3,4}$ are real if and only if $e^{\theta} < 2/\sqrt{3}$, i.e., $\theta \lesssim 0.144$. If the latter condition is violated, then $\lambda_{3,4}(k)$ acquire a nonzero real part, and constant-amplitude solutions (and, respectively, the soliton solutions on the constant-amplitude background) become unstable with respect to small-wavelength ($|k| \gg 1$) perturbations. Systematic numerical evaluation of roots of the characteristic equation indicates that below the found instability threshold the constant-amplitude waves are stable.

In the region where the modulational instability is absent, we perform an additional search for possible unstable modes by numerical solutions of the linear stability equations (18). It indicates that below the modulational instability threshold the dark-gray solitons are stable, except for a narrow parametric interval of weak instabilities centered around $v_s = 1/2$. Bright solitons on the pedestal are unstable even below the modulational instability threshold due to the presence of internal unstable modes associated with localized eigenfunctions of the linear-instability operator.

D. Gray-gray solitons

Phase portrait in Fig. 2(c) indicates that when the constant of integration C in Eq. (8) is nonzero, the bright solitons on the pedestal coexist with gray solitons, i.e., nontopological dips in the constant-amplitude background, with the amplitude at the dip being nonzero. While the shape of the bright solitons is similar to those presented in the previous subsection, the gray-gray solitons constitute a significant generalization of the dark-gray solitons presented above. The respective solutions can also be found in analytical form, although the resulting expressions are rather bulky. To simplify the presentation, in this subsection we set $\kappa = g = 1$. Then the amplitude and phase of the excitonic field is given as

$$\rho_s(\zeta) = \rho_\infty\sqrt{\frac{\sinh^2(p\zeta) + c}{\cosh^2(p\zeta) - b}} \tag{38}$$

and

$$\Theta_s(\zeta) = \int_0^\zeta \left(\frac{3}{4v_s}\rho_s^2 + C\rho_s^{-2}\right)d\zeta' = \frac{\pi}{2p}\left(\frac{3\rho_\infty^2}{4v_s}\cos^2 s_2\tan s_1 + \frac{C}{\rho_\infty^2}\cos^2 s_1\tan s_2\right) + \frac{3\rho_\infty^2}{4v_s}\left(\zeta - \frac{\sin^2 s_2\cot s_1}{p}\arctan[\tan(s_1)\tanh(p\zeta)] - \frac{\cos^2 s_2\tan s_1}{p}\arctan[\cot s_1\coth(p\zeta)]\right) + \frac{C}{\rho_\infty^2}\left(\zeta - \frac{\sin^2 s_1\cot s_2}{p}\arctan[\tan(s_2)\tanh(p\zeta)] - \frac{\cos^2 s_1\tan s_2}{p}\arctan[\cot s_2\coth(p\zeta)]\right), \tag{39}$$

TABLE I. Three numerical sets for gray-gray and bright solitons on constant-amplitude background presented in Sec. II D. Values v_s, ρ_∞, and δ_s are exact, and values in other columns are approximate; subscripts *gray* and *bright* correspond to parameters for the coexisting gray-gray and bright solitons.

No.	v_s	ρ_∞	δ_s	C	p	b_{gray}	c_{gray}	b_{bright}	c_{bright}
1	0.25	0.5	1.07	0.0506	1.0946	0.0466	0.0301	0.9534	0.9699
2	0.5	0.5	1.14	0.0557	0.6881	0.0264	0.0899	0.9735	0.9101
3	0.75	1	1.2	0.7080	1.1396	0.0440	0.2547	0.9560	0.7453

where $s_1 = \arcsin\sqrt{b}$ and $s_2 = \arccos\sqrt{c}$. For negative ζ, $\Theta_s(\zeta)$ must be redefined as an odd function: $\Theta_s(\zeta) := -\Theta_s(-\zeta)$. Then the solution can be found as

$$\psi_s(\zeta) = \rho_s(\zeta)\exp\left[i\Theta_s(\zeta) - i\zeta\frac{\delta_s(1-2v_s)}{2v_s(1-v_s)}\right]. \tag{40}$$

Analytical expressions for constant p, b, and c are available in a computer algebra program, but are too bulky to be presented herein. Instead, in Table I we present three numerical sets for gray and bright solitons with different velocities.

III. DIRECT NUMERICAL MODELING OF SOLITON DYNAMICS

Now let us consider the dynamical development of the instabilities of the soliton solutions discussed above. The numerical simulations of the field evolution are done by well known split-step method. At the first step, we solve a linear part of the equation in Fourier space and, at the second step, we solve the nonlinear part. The typical step of the spatial mesh was about $\Delta x = 10^{-3}$ and the time step $\Delta t = 10^{-4}$. The boundary conditions are periodic, the width of the simulation window L is much larger than the soliton width ($L \approx 30$). In the case of the solitons on a background, the width of the window was adjusted to provide the continuity of both fields at all points of the simulation interval. It was specially checked that neither spatial no temporal discretizations affected the results of the simulations.

We start with the bright solitons without a background. Numerical study in Sec. II B has indicated that the solitons are stable when the soliton frequency δ_s is negative [which in terms of the parametrization adopted in Eqs. (12) corresponds to $\theta > 0$], but become unstable for negative θ, and the emerging instabilities are initially rather weak, which makes it difficult to detect precisely the instability threshold. These findings agree with the results of numerical simulations of soliton dynamics presented in Fig. 5. The initial conditions were taken in the form of a soliton perturbed by a weak noise in both A and ψ fields. As one can see for positive $\theta = 0.1$ the soliton is stable and this complies with the results of the spectral stability analysis. At negative θ the soliton becomes unstable and the instability growth rate increases with at higher absolute values of θ. Relatively weak instabilities feature a "radiative" behavior which corresponds to a poorly localized in space unstable eigenfunction. Stronger instabilities, such as those with $\theta = -1$ in Fig. 5, cause the complete destruction of the solitons at relatively short times.

To compare the results of the direct numerical simulations with the predictions of the linear stability analysis obtained from the numerical solution of the spectral problem (18), we have extracted the growth rate and the oscillation frequency of the perturbation destroying the solitons. The results of the numerical simulations are summarized in Figs. 6(a)–6(c) for $\theta = -0.6$. We take the initial conditions in the form of analytical soliton solution perturbed by a weak noise. Then we perform numerical simulation and for each moment of time evaluate the perturbation on the soliton background. The perturbation is defined as $\vec{U}(x,t) = (A(x,t) - A_s(x-\xi)\exp(i\Phi), \psi(x,t) - \psi_s(x-\xi)\exp(i\Phi))^T$ with the phase Φ and the displacement ξ giving the minimum of the norm $N = \int |\vec{U}|^2\, dx$ (here A_s, ψ_s are the analytical solution, A and ψ are the fields distributions found by numerical simulations). A typical evolution of the perturbation $\vec{U}$ is shown in Fig. 6(a) showing the spatiotemporal evolution of $|\vec{U}|^2$ in the reference frame moving with the soliton. The oscillatory growth of the perturbation is clearly seen in this figure. Figure 6(b) shows the dynamics of the norm N in logarithmic scale. It is seen that after some time, when the growing mode start dominating over other components of the perturbation, the norm N grows exponentially in time. This allows us to extract the growth

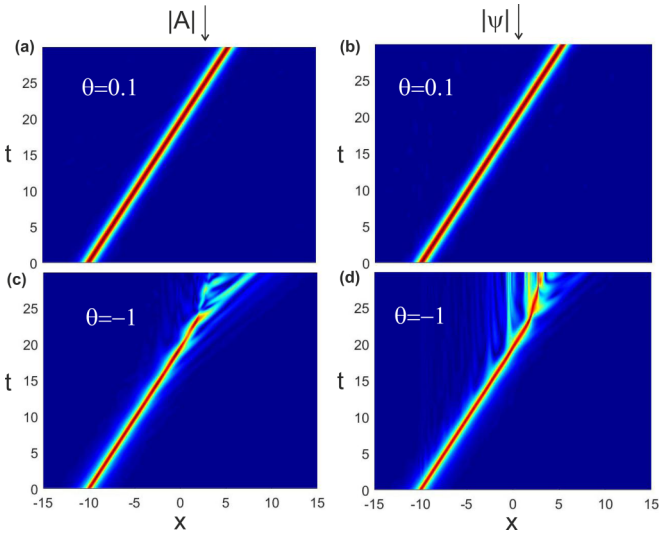

FIG. 5. The evolution of a stable (a, b) and an unstable (c, d) bright solitons. Panels (a, c) are for A fields and panels (b, d) are for ψ fields. The initial conditions for the simulations are taken in the form of a soliton solution perturbed by a weak noise. Soliton parameters are $\alpha = 0.8$ and $\theta = 0.1$ (stable soliton), $\theta = -1$ (unstable soliton).

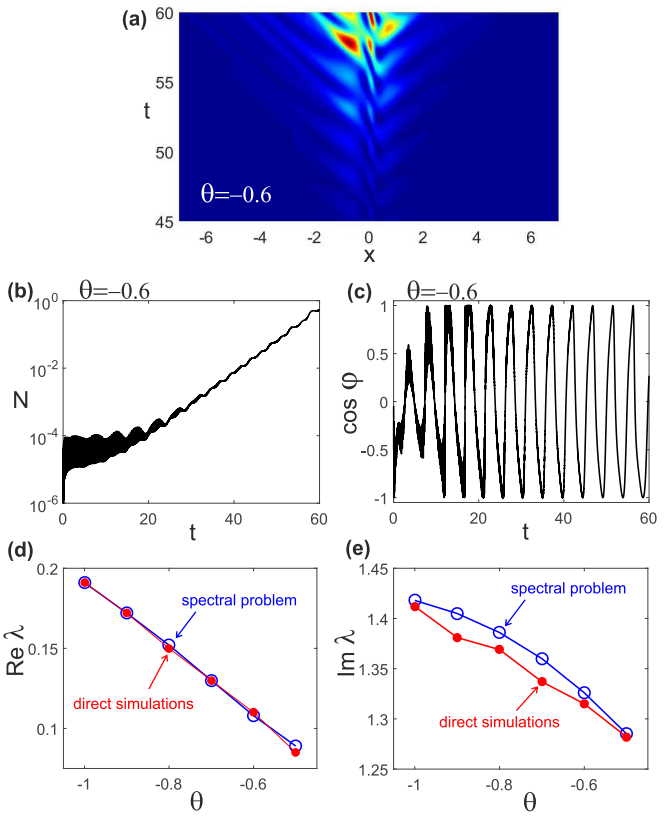

FIG. 6. The evolution of a perturbation growing from the weak noise imposed over an unstable bright soliton solution is shown in panel (a) for $\theta = -0.6$ and $\alpha = 0.8$. Panel (b) illustrates the growth of the norm of the perturbation. Panel (c) shows the temporal evolution of the cosine of the mutual phase φ of the soliton and the perturbation calculated at the point of the soliton intensity maximum. The values of the real and imaginary parts of the eigenfunctions governing the dynamics of the unstable perturbation are given in panels (d) and (e) for different values of θ. The eigenvalues found by the solution of the spectral eigenvalue problem are shown by open blue circles; the eigenvalues extracted from direct numerical simulations are shown by red circles. The thin lines in these panels are just guides for the eye.

rate from the results of numerical simulations. We can also calculate the mutual phase between the soliton and the perturbation defined as $\varphi = \arg U_1(x_m, t)$ where U_1 is the first component of $\vec{U}$ and x_m is the coordinate of the maximum of the field intensity distribution. The temporal behavior of $\cos\varphi$ is shown in Fig. 6(c). At larger t the dependency becomes quasisinusoidal and its inverse period gives an estimate for the imaginary part of the eigenvalue (the frequency) of the growing perturbation.

This way we can compare the growth rates (real parts of λ) and the frequencies (imaginary parts of λ) of the growing perturbations obtained from direct numerical modeling and from numerical solution of the spectral problem. These values are shown in Figs. 6(d) and 6(e) for different values of θ. One can see a good quantitative agreement between the eigenvalues. Therefore the results of numerical simulations support the conclusion on the presence of oscillatory instabilities in linear-instability spectra of bright solitons.

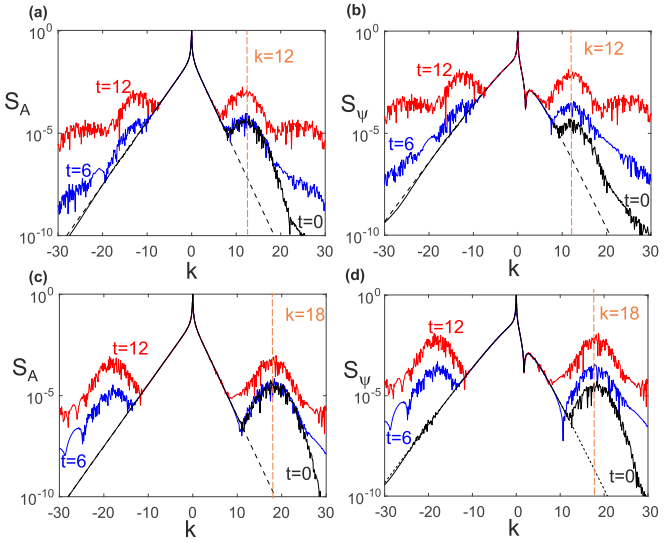

FIG. 7. The spectra of A and ψ fields are shown in log scale in panels (a, c) and (b, d) correspondingly. The initial conditions are taken in the form of the dark-gray soliton perturbed by a weak noise. The spectrum of the noise is a Gaussian function of the width $w_s = 3$ centered at $k = 12$ in (a) and (b) and $k = 18$ in (c) and (d). The positions of the centers of noise spectra are marked by the dashed orange lines labeled as $k = 12$ and $k = 18$. The dark line shows the spectra of the initial fields; the black dashed curves are the soliton spectra with the parameters $\alpha = \pi/6$ and $\theta = 0.25$. The spectra at $t = 6$ and $t = 12$ are shown by the blue and the red lines.

Now we proceed to various solitons that nestle on a background of constant nonzero amplitude. According to the results of Sec. II C, eventual instability of these solutions can originate either in the modulational instability of the constant-amplitude background or in internal unstable modes of the soliton itself. In order to illustrate the instability of the former type, we consider a dark-gray soliton nestling on an unstable background. In this case the unstable modes can be characterized by a wave vector because far away of the soliton core the asymptotical behavior of the eigenfunctions corresponds to plane waves. The spectral analysis shows that all modes with relatively high k are unstable. So to demonstrate the instability and be sure that the numerical method is valid, we take the noise with localized spatial spectrum and check that at

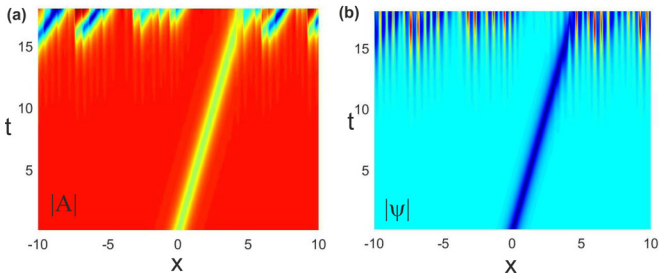

FIG. 8. The temporal evolutions of A and ψ fields are shown in panels (a) and (b). The initial distributions of the fields are taken in the form of the soliton solution with $\alpha = \pi/6$ and $\theta = 0.25$ perturbed by a weak noise having the Gaussian spectrum of width $w_s = 3$ centered at $k = 12$.

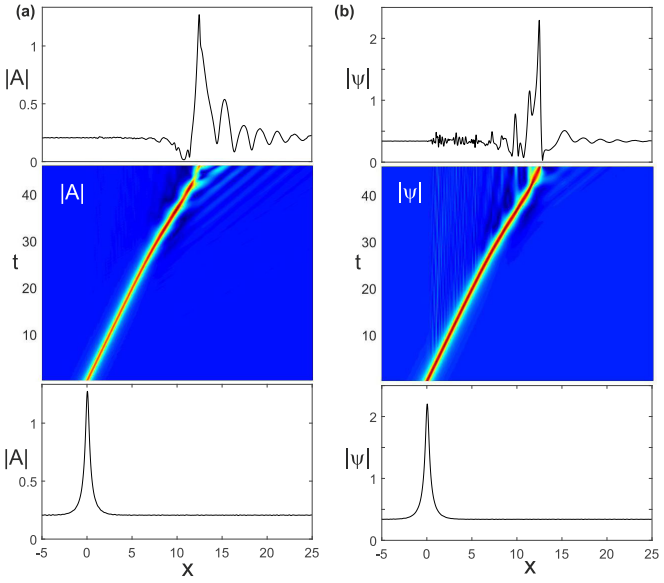

FIG. 9. The decay of a bright soliton on the background. Panel (a) shows the initial distribution of A field (lower part), the evolution of the field (in the middle), and the field distribution at $t = 46$ (the upper part). Panel (b) shows the same for ψ field. The initial conditions for the simulations are taken in the form of a soliton solution perturbed by a weak noise. Soliton parameters are $\alpha = \pi/6$ and $\theta = 0.05$ [see Eqs. (26) for the adopted parametrization].

large simulation times we do not see the growth of the modes with very high k and thus our discretization does not affect the results of the simulations. To this end, we prepare the initial random perturbation as follows: we take random field distribution, calculate its Fouirer transform, multiplied it with a Gaussian function centered at some k, and then calculate the inverse Fourier transform. The spectra of A and ψ fields at different propagation times are shown in Fig. 7. The spectra of the initial distribution are shown by black lines. The spectra of pure soliton solutions are shown as a reference by a dashed black lines. We observe that the perturbation grows and the satellite spectral lines appear. At large times the instability destroys the background and, correspondingly, destroys the solitons; see Fig. 8 illustrating this process.

We have also examined the stability of bright solitons on a pedestal that are another kind of possible localized solutions. These solitons are unstable even below the modulational

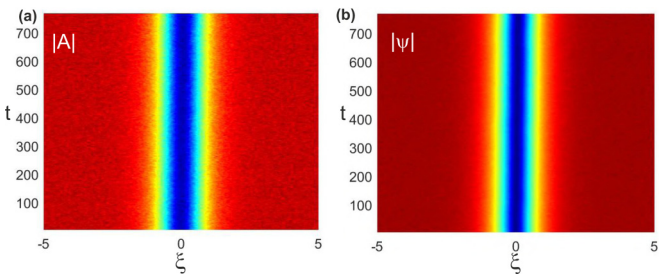

FIG. 10. The evolutions of A (a) and ψ (b) fields are shown for a generalized gray soliton. The horizontal axis $\xi = x - v_s t$ where v_s is the velocity of the analytically found soliton. The numerical soliton parameters correspond to No. 1 in Table I.

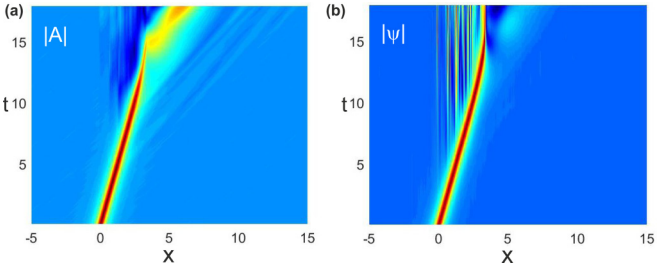

FIG. 11. The evolutions of A (a) and ψ (b) fields are shown for a generalized bright soliton. The numerical soliton parameters correspond to No. 1 in Table I.

instability threshold because of the presence of spatially localized unstable modes. This dynamical instability is illustrated in Fig. 9 showing the decay of these solitons into dispersive waves envelope overlapped with the background.

To continue, we have investigated the behavior of generalized, gray-gray solitons found in Sec. II D. The numerical simulations confirm that these solitons can be stable. Fig. 10 shows the evolution of a perturbed gray-gray soliton in a reference frame moving at the velocity of the unperturbed solitons. The use of the moving reference frame allows us to notice small variations in the shape and small displacement of the solitons. However the perturbations do not grow indicating that the solitons are stable. This means that the results of direct numerical simulations are in agreement with the prediction of the linear spectral analysis discussed above. Thus one can conclude that the gray-gray solitons are stable provided that their constant-amplitude background is stable. Finally, we have also checked the dynamics of the generalized bright solitons for the three cases listed in Table I. The simulations show that all bright solitons are unstable and get destroyed in a similar manner; see Fig. 11 showing a typical spatial-temporal evolution of the A and ψ fields. The instability is presumably of radiative kind, at first the perturbations growth in ψ field, cascading and making the spatial spectrum wider. Then it affects the A field causing complete destruction of the soliton.

IV. CONCLUSION

In this work, we have thoroughly investigated, analytically and numerically, different families of the solitons that exist in the experimentally relevant model describing the evolution of optical pulses in the conservative systems with strong light-matter coupling. In particular, we found analytically the solutions for bright solitons on zero and nonzero backgrounds (solitons on pedestal), Ising-like dark solitons having a point where the excitonic field intensity is exactly zero and the phase of the field shifts by π and gray (Bloch-like) solitons where the intensity has a dip and the phase of the field is continuous and rotates in the soliton core. The corresponding two-component solutions can be termed to as dark-gray ("half-topological") and gray-gray (nontopological) solitons. All found solutions coexist in the system but, in a properly defined linear limit, detach from different polariton branches of the dispersion law: bright solitons bifurate from the lower branch towards the gap, and all other solutions detach from the upper branch.

We have found that stability of bright solitons on zero background can be affected by oscillatory (radiative) instabilities which emerge when the soliton frequency becomes positive. The oscillatory instability increment is initially weak, but grows distinctively as the soliton frequency increases. Instability of the solitons on the nonzero background can develop either from the modulational instability of the constant-amplitude waves or from the internal unstable modes. All examined bright-bright solitons are unstable, while dark-gray and gray-gray solitons are stable in vast parametric regions below the modulational instability threshold. The stability predictions, including the prominent role of the radiative instability, have been verified in direct numerical modeling of soliton dynamics.

The results of the paper shed light on possible localized solutions that may exist in the conservative system with strong light-matter coupling when only material excitations are nonlinear. The variety of found analytical solutions can be used as a starting point for developing a perturbation theory for the dissipative and driven-dissipative systems where the dissipative terms can be considered as perturbations. We believe that this will facilitate the theoretical studies of the hybrid systems with light-matter interactions.

ACKNOWLEDGMENT

The research was supported by Priority 2030 Federal Academic Leadership Program.

[1] A. Hasegawa and F. Tappert, Transmission of stationary nonlinear optical pulses in dispersive dielectric fibers, Appl. Phys. Lett. **23**, 142 (1973).

[2] L. F. Mollenauer, R. H. Stolen, and J. P. Gordon, Experimental Observation of Picosecond Pulse Narrowing and Solitons in Optical Fibers, Phys. Rev. Lett. **45**, 1095 (1980).

[3] H. A. Haus and W. S. Wong, Solitons in optical communications, Rev. Mod. Phys. **68**, 423 (1996).

[4] J. M. Dudley, G. Genty, and S. Coen, Supercontinuum generation in photonic crystal fiber, Rev. Mod. Phys. **78**, 1135 (2006).

[5] D. V. Skryabin and A. V. Gorbach, Looking at a soliton through the prism of optical supercontinuum, Rev. Mod. Phys. **82**, 1287 (2010).

[6] N. N. Akhmediev and A. Ankiewicz, *Solitons: Nonlinear Pulses and Beams* (Chapman & Hall, New York, 1997).

[7] Y. S. Kivshar and G. P. Agrawal, *Optical Solitons: From Fibers to Photonic Crystals* (Academic Press, San Diego, 2003).

[8] I. Carusotto and C. Ciuti, Quantum fluids of light, Rev. Mod. Phys. **85**, 299 (2013).

[9] I. Carusotto and C. Ciuti, Probing Microcavity Polariton Superfluidity through Resonant Rayleigh Scattering, Phys. Rev. Lett. **93**, 166401 (2004).

[10] P. M. Walker, L. Tinkler, D. V. Skryabin, A. Yulin, B. Royall, I. Farrer, D. A. Ritchie, M. S. Skolnick, and D. N. Krizhanovskii, Ultra-low-power hybrid light-matter solitons, Nat. Commun. **6**, 8317 (2015).

[11] P. M. Walker, L. Tinkler, B. Royall, D. V. Skryabin, I. Farrer, D. A. Ritchie, M. S. Skolnick, and D. N. Krizhanovskii, Dark Solitons in High Velocity Waveguide Polariton Fluids, Phys. Rev. Lett. **119**, 097403 (2017).

[12] C. M. de Sterke and J. E. Sipe, Gap solitons, Prog. Opt. **33**, 203 (1994).

[13] K. I. Pushkarov, D. I. Pushkarov, and I. V. Tomov, Self-action of light beams in nonlinear media: soliton solutions, Opt. Quantum Electron. **11**, 471 (1979); L. Gagnon, Exact traveling-wave solutions for optical models based on the nonlinear cubic-quintic Schrödinger equation, J. Opt. Soc. Am. A **6**, 1477 (1989); D. Pushkarov and S. Tanev, Bright and dark solitary wave propagation and bistability in the anomalous dispersion region of optical waveguides with third- and fifth-order nonlinearities, Opt. Commun. **124**, 354 (1996); S. Tanev and D. I. Pushkarov, Solitary wave propagation and bistability in the normal dispersion region of highly nonlinear optical fibres and waveguides, *ibid.* **141**, 322 (1997).

[14] I. V. Barashenkov, D. E. Pelinovsky, and E. V. Zemlyanaya, Vibrations and Oscillatory Instabilities of Gap Solitons, Phys. Rev. Lett. **80**, 5117 (1998).

[15] P. J. Y. Louis, E. A. Ostrovskaya, C. M. Savage, and Y. S. Kivshar, Bose Einstein condensates in optical lattices: Bandgap structure and solitons, Phys. Rev. A **67**, 013602 (2003); N. K. Efremidis and D. N. Christodoulides, Lattice solitons in Bose-Einstein condensates, *ibid.* **67**, 063608 (2003); D. E. Pelinovsky, A. A. Sukhorukov, and Y. S. Kivshar, Bifurcations and stability of gap solitons in periodic potentials, Phys. Rev. E **70**, 036618 (2004); P. P. Kizin, D. A. Zezyulin, and G. L. Alfimov, Oscillatory instabilities of gap solitons in a repulsive Bose Einstein condensate, Physica D **337**, 58 (2016).

[16] D. E. Pelinovsky, A. V. Buryak, and Y. S. Kivshar, Instability of Solitons Governed by Quadratic Nonlinearities, Phys. Rev. Lett. **75**, 591 (1995); A. V. Buryak, Y. S. Kivshar, and S. Trillo, Stability of Three-Wave Parametric Solitons in Diffractive Quadratic Media, *ibid.* **77**, 5210 (1996).